A Fine-Grained Intelligent Mesh Quality Evaluation Algorithm Based on Neural Networks

Ke Yang[1,2,3], Xinhai Chen[1,2,3,*], Zhichao Wang[1,2,3], Qinglin Wang[1,2,3] and Jie Liu[1,2,3]
[1]Laboratory of Digitizing Software for Frontier Equipment,
National University of Defense Technology, Changsha 410073, China
[2]National Key Laboratory of Parallel and Distributed Computing,
National University of Defense Technology, Changsha 410073, China
[3]College of Computer Science and Technology,
National University of Defense Technology, Changsha 410073, China
[*]Corresponding Author: Xinhai Chen, Email: chenxinhai16@nudt.edu.cn

***Abstract*—Mesh quality is a fundamental factor in large-scale scientific computing, serving as a critical bridge between physical modeling and numerical simulation which dictates the accuracy and stability of numerical solutions. Traditional mesh quality evaluation primarily relies on handcrafted geometric metrics and expert experience, which often requires extensive manual intervention and high preprocessing costs. While recent intelligent methods offer efficient and automated evaluation, they are restricted to mesh-level evaluation—judging only the overall quality of a mesh—and lack the capability to precisely locate individual low-quality elements. To bridge this gap, we first introduce NACA-FineGrade, the pioneering mesh dataset featuring element-level annotations. Building upon this benchmark, we further propose a fine-grained intelligent evaluation algorithm, termed FG-MeshNet, which enables the precise localization and identification of localized mesh defects. Specifically, FG-MeshNet employs a dedicated three-channel mesh representation, integrated with multi-branch segmentation heads and a collaborative attention mechanism to effectively capture multi-scale structural features. Experimental results demonstrate that FG-MeshNet attains 89.3% accuracy, surpassing existing methods by enabling reliable element-level diagnostics that precisely identify and localize critical geometric defects, such as poor orthogonality, insufficient smoothness, and uneven density.**

***Index Terms*—Computational Fluid Dynamics, Mesh Quality Evaluation, Instance Segmentation**

I. Introduction

In scientific computing, mesh quality is fundamental to the accuracy and efficiency of numerical simulations across diverse fields, including electromagnetics and structural mechanics [1]. Poor-quality meshes can introduce significant discretization errors and deteriorate the condition number of the system matrix, thereby restricting solver convergence speed or even leading to numerical divergence. Specifically, geometric defects such as high aspect ratios and large skew angles degrade interpolation accuracy and impair the capture of physical fields in regions with sharp gradients. In structural analysis, this manifests as distorted stress distributions, while in fluid and electromagnetic simulations, it results in misrepresented physical structures and unreliable predictive results.

Given the profound impact of mesh quality on numerical stability, mesh quality evaluation has become an indispensable step in the pre-processing phase. Effectively identifying mesh defects prior to computation can prevent costly post-computation error analysis and numerical failure. Traditional evaluation methods primarily rely on constructing systematic quantitative metrics based on the geometric characteristics of elements. For instance, structured meshes often utilize the vertex volume ratio or Jacobian determinant to measure regularity, while unstructured meshes focus on geometric integrity through metrics such as skewness and adjacent element size ratios. Although these geometric metrics provide an intuitive way to screen for distortion and stretching, they suffer from a lack of clear quantitative correlation with final simulation accuracy [2]. Furthermore, the traditional evaluation paradigm relies heavily on manual expert experience and cumbersome human-computer interaction, leading to high preprocessing costs and limited automation in complex engineering workflows [3].

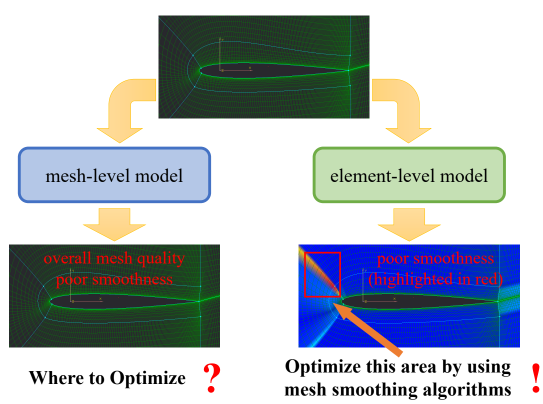

Fig. 1. Comparison between mesh-level and element-level evaluation.

In recent years, intelligent mesh quality evaluation has emerged as a prominent research topic, with numerous studies leveraging CNNs, GNNs, and Transformers to automate eval-

This research was partially supported by the National Natural Science Foundation of China (12402349), the Natural Science Foundation of Hunan Province (2024JJ6468), the Innovation Reserch Foundation of National University of Defense Technology (ZK2023-11), and the National Key Research and Development Program of China (2021YFB0300101).

uation [4]–[10]. While these methods have made significant progress, they are primarily restricted to mesh-level evaluation. This coarse-grained approach creates a "black box" bottleneck, as current models—functioning largely as global classifiers—fail to locate individual low-quality elements or provide actionable guidance for mesh repair. Consequently, as illustrated in Fig. 1, a transition from mesh-level to element-level evaluation is essential to bridge this gap and enhance the automation of CFD pre-processing.

To bridge the gap from coarse-grained mesh-level assessment to precise element-level evaluation, this paper proposes a fine-grained intelligent algorithm that enables the exact localization and identification of mesh defects, thereby overcoming the "black box" limitations inherent in existing methods. To the best of our knowledge, this work is the first to achieve element-level evaluation of mesh quality. Our core contributions are three-fold:

- We establish the first publicly available mesh dataset, NACA-FineGrade, with element-level quality annotations, filling the data gap in the field of fine-grained mesh quality evaluation.
- We propose FG-MeshNet, a novel mesh quality evaluation algorithm that achieves state-of-the-art performance. By incorporating multi-scale perception and collaborative attention mechanisms, the model enables the precise identification of low-quality regions, offering an effective and automated solution for mesh quality assessment.
- We validate the effectiveness of the proposed modules in enhancing model discrimination accuracy and robustness through systematic module ablation and comparative experiments.

II. Related work

A. Mesh quality evaluation

Evaluating mesh quality is a complex and non-trivial task. While post-computation analysis is intuitive, high costs often make it impractical. Consequently, the prevailing practice is to conduct a mesh pre-evaluation prior to computation. In the mesh generation workflow, quality metrics are widely employed to identify defects, such as geometric distortions or topological errors. This approach is essential for the rapid screening of large-scale 3D meshes. Existing methods can be broadly categorized into traditional and intelligent methods.

1) Traditional mesh quality evaluation methods: Traditional methods primarily utilize geometric metrics to assess numerical accuracy and stability [11]. For structured meshes, ICEM-CFD uses the vertex volume ratio ($Q_{\text{ICEM}} = V_{\min}/V_{\max}$) to measure regularity, while Pointwise relies on the Jacobian determinant. For unstructured meshes, evaluation emphasizes geometric integrity, including positive volume, face coplanarity, and controlled size ratios. Additionally, the volume-weighted gradient (∇h) assesses size smoothness.

Recent trends have shifted the evaluation objective from "geometric perfection" toward "computational suitability." Nguyen-Dinh et al. [12] proposed a goal-oriented evaluation method based on total derivative information; unlike traditional geometric strategies, this approach assesses the mesh's impact on target results using the derivatives of functional quantities. Similarly, Gao et al. [2] evaluated hexahedral metrics through correlation analysis, finding that element condition number metrics are more representative of simulation accuracy and stability than the commonly used Jacobian matrix.

2) Intelligent mesh quality evaluation methods: Intelligent mesh evaluation methods automatically learn quality evaluation patterns from data, overcoming the limitations of traditional metric-based approaches. Modern techniques using GNNs and CNNs have established end-to-end evaluation by processing geometric and topological information, making them particularly effective for complex mesh structures.

Chen et al. [4] pioneered deep learning-based mesh evaluation with GridNet on the NACA-Market dataset, later proposing the lightweight MQNet [5] to improve efficiency via depthwise separable convolution. Wang et al. [6] introduced GMeshNet, utilizing Graph Neural Networks and multi-level fusion to extract topological features. Building upon this, Liu et al. [7] employed Transformer architectures with W-MSA and SW-MSA to capture local and global features. Alternatively, Zhang et al. [8] reformulated the task as a multi-label problem to avoid interference from correlations between categories.

To expand the engineering applicability of deep learning, Chen et al. [9], [10] proposed several point cloud-based networks for 3D mesh evaluation. Their initial work [9] featured a two-stage network for local and global discrimination, supported by a public dataset of 24,576 samples. For 3D cylindrical structures, the Mesh-Net [10] architecture was introduced to capture multi-scale features from multi-size inputs. Additionally, Chen et al. [13] developed AircraftNet, which employs a CellConv extractor to capture nonlinear geometric features in unstructured meshes.

Despite these advancements, existing methods remain constrained to mesh-level quality evaluation and lack the capability for element-level defect localization, rendering them unable to guide mesh optimization and thus severely restricting their practical utility in engineering practice.

B. Instance segmentation

Instance segmentation combines object detection and semantic segmentation for pixel-level recognition, serving as a core technology for autonomous driving and robotics. Methods are primarily categorized into "top-down" and "bottom-up" paradigms. Representative top-down works like Mask R-CNN [14] utilize RoIAlign for localization followed by segmentation, while subsequent models such as PANet [15] and Hybrid Task Cascade [16] strengthen feature aggregation and task interaction.

Conversely, bottom-up methods learn pixel embeddings or location encodings [17] to distinguish instances through clustering after semantic segmentation; however, while offering high mask resolution, these approaches often involve complex post-processing and exhibit lower accuracy in complex scenes compared to detection-based methods. Recently, single-stage models have garnered attention for their real-time potential, with YOLACT [18] achieving efficiency by decoupling prototype mask generation from coefficient prediction, while BlendMask [19] strikes a favorable balance between accuracy and speed by fusing high-level instance information with low-level details. Drawing inspiration from these advancements, we formulate fine-grained mesh quality evaluation as an instance segmentation task, specifically aimed at isolating and identifying individual low-quality mesh elements.

III. Dataset and method

A. Data preparation

1) NACA-FineGrade dataset generation: High-quality datasets are essential for intelligent mesh evaluation, yet the lack of fine-grained annotations remains a bottleneck, hindering element-level evaluation and automated optimization. To bridge this gap, we developed NACA-FineGrade—the first large-scale, element-level mesh dataset. This benchmark features NACA-0009 and NACA-6510 airfoils across C-type and H-type topologies, providing a refined foundation for detailed, high-fidelity defect analysis. Representative illustrations of these airfoils and topologies are shown in Fig. 2.

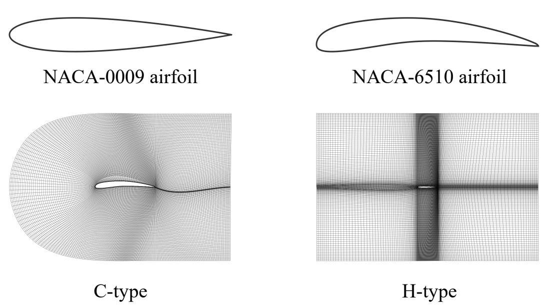

Fig. 2. Two different airfoil models and mesh topologies used in NACA-FineGrade.

Using the GridStar software, we systematically adjust key parameters – including the first layer height of the boundary layer (ranging from 1×10^{-5} to 8×10^{-1}), mesh line deflection angle (-30° to 30°), and distribution length – via automated scripts to batch-generate mesh samples covering various potential quality defects. The detailed configuration of airfoils, topologies, dimensions ranges, and sample numbers is summarized in Table I.

TABLE I
Dataset composition of NACA-FineGrade.

Airfoil	Topology	Dimensions Range	Number
NACA-0009	C-Type	80×380, 82×384, ..., 98×416	10240
	H-Type	80×500, 80×501, ..., 80×509	10240
NACA-6510	C-Type	80×380, 82×384, ..., 98×416	10240
	H-Type	80×500, 80×501, ..., 80×509	10240

During the annotation process, we perform element-level identification and classification of substandard quality regions within each mesh. Specifically, for each local region exhibiting a quality defect, we annotate its defect category, covering the three core quality attributes – $orthogonality$, $smoothness$, and $density$ – and their combinations, as illustrated in Fig. 3.

NACA-FineGrade comprises 40,960 mesh samples, with 10,240 per topology–airfoil combination. The dataset covers orthogonality, smoothness, and density defects, which frequently exhibit spatial intersections and multi-label coexistence. This complexity, combined with defect scales ranging from localized flaws to macroscopic issues, ensures robust model discrimination. By providing detailed element-level annotations, NACA-FineGrade establishes a solid foundation for algorithms to achieve precise defect localization and classification, thereby facilitating automated mesh repair strategies.

2) Mesh representation: We adopt a 2D geometric quantization strategy to overcome the limitations of traditional nodal representations, such as spatial coordinates or the Signed Distance Function, which provide only sparse local information. By extracting key geometric characteristics directly from mesh elements, this strategy provides comprehensive geometric context while reducing the reliance on computationally expensive message-passing operations.

The specific procedure is as follows (see Fig. 4): First, three key geometric features are extracted for each mesh element—the edge length along the x-direction l_x, the edge length along the y-direction l_y, and the element's maximum internal angle $\theta_{\max}$. This maps each element to a three-dimensional feature vector $\mathbf{f} = [l_x, l_y, \theta_{\max}]^T$. Subsequently, based on the mesh's topological connectivity, the feature vectors of each element are arranged into a matrix format according to their spatial positions, constructing a three-channel input matrix $\mathbf{M} \in \mathbb{R}^{H \times W \times 3}$, where H and W represent the number of rows and columns in the mesh's structural layout, respectively. This matrix encodes the structured representation of the underlying airfoil mesh, embedding irregular geometric information into a regular data structure, effectively overcoming the limitations of traditional pixel representations when handling non-uniform meshes.

After constructing the mesh representation, to unify the numerical scales of features across different channels and enhance the convergence and stability of neural network training, this study applies normalization strategies aligned with the physical characteristics of each geometric feature. Specifically, for the edge lengths l_x and l_y representing element size, maximum value normalization is applied to preserve their inherent proportional relationship:

$$\hat{l}_x = \frac{l_x}{l_{\max}}, \quad \hat{l}_y = \frac{l_y}{l_{\max}}, \tag{1}$$

where $l_{\max} = \max(l_x, l_y)$ is the maximum value of the corresponding edge length for each element. For the maximum internal angle feature $\theta_{\max}$, Min-Max normalization is used to map it to the $[0, 1]$ interval:

$$\hat{\theta}_{\max} = \frac{\theta_{\max} - \theta_{\min}^{\text{global}}}{\theta_{\max}^{\text{global}} - \theta_{\min}^{\text{global}}}, \tag{2}$$

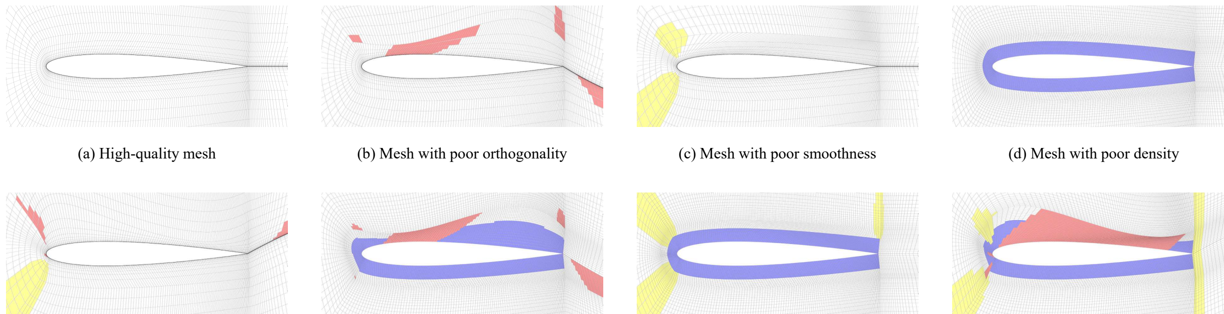

(a) High-quality mesh (b) Mesh with poor orthogonality (c) Mesh with poor smoothness (d) Mesh with poor density

(e) Mesh with poor orthogonality and smoothness (f) Mesh with poor orthogonality and density (g) Mesh with poor smoothness and density (h) Poor-quality mesh

Fig. 3. Examples of generated NACA-0009 airfoil mesh samples in NACA-FineGrade. Defect types are color-coded: poor orthogonality (red), poor smoothness (yellow), and poor density (blue).

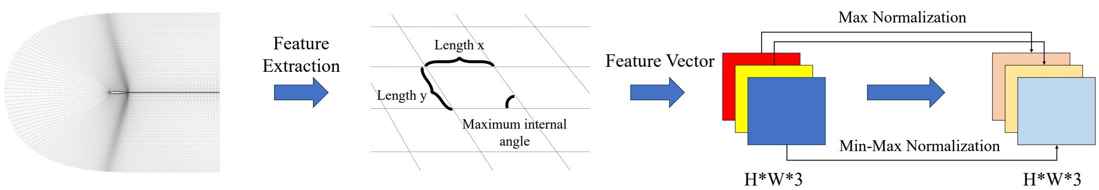

Fig. 4. Mesh workflow characterization.

where $\theta_{\min}^{\text{global}}$ and $\theta_{\max}^{\text{global}}$ are the minimum and maximum values of the maximum internal angle among all elements in the training set, respectively. Finally, the normalized three-channel matrix $\hat{\mathbf{M}} = \text{Stack}(\hat{l}_x, \hat{l}_y, \hat{\theta}_{\max})$, where $\hat{\mathbf{M}} \in \mathbb{R}^{H\times W\times 3}$, serves as the input to the neural network for the subsequent fine-grained mesh element quality instance segmentation task.

B. The FG-MeshNet algorithm

To achieve element-level mesh quality evaluation, we propose the FG-MeshNet algorithm, a specialized deep learning method designed based on the instance segmentation paradigm. By integrating multi-scale perception and a multi-dimensional cooperative attention mechanism, this algorithm effectively addresses the challenge of identifying localized defects.

1) Overall algorithm design: Designing FG-MeshNet for element-level mesh quality evaluation requires balancing global topological structures and microscopic geometric defects. To this end, we adopt the YOLOv8 [20] architecture as our structural baseline, leveraging its proven capability in multi-scale feature fusion and high-precision object localization. FG-MeshNet processes a $640 \times 640 \times 3$ feature tensor through four core components depicted in Fig. 5: a feature extraction backbone, a bidirectional feature fusion neck, a decoupled segmentation head, and a prototype mask generation branch.

The backbone transforms structured meshes into a normalized three-channel matrix via a padding strategy. It utilizes a four-stage downsampling architecture with C3 modules to extract hierarchical geometric features, outputting feature maps of $160 \times 160 \times 32$, $80 \times 80 \times 64$, $40 \times 40 \times 128$, and $20 \times 20 \times 256$. SPPF and Multi-dimensional Cooperative Attention (MCA) [21] modules are integrated at the backbone's end to further enhance global context representation. Following extraction, the bidirectional neck facilitates interaction between multi-scale features to identify sparse, variable-sized low-quality elements.

The network culminates in a decoupled segmentation head, where each scale of the feature pyramid performs category classification, 32-dimensional mask coefficient prediction, and Wise-IoU (WIoU) v3 [22]-based bounding box regression to improve localization for irregular defect boundaries. In parallel, a prototype generation branch produces a $160 \times 160 \times 32$ global prototype mask. The final fine-grained quality mask for each element is generated by a linear combination of the predicted mask coefficients and the prototype tensor, followed by Sigmoid activation.

2) MCA module: The FG-MeshNet integrates an MCA module at the backbone's terminal stage to enhance feature representation for mesh quality evaluation. This lightweight module models attention across channel, height, and width dimensions efficiently, facilitating precise localization of low-quality mesh regions. The detailed structure of the MCA module is illustrated in Fig. 6.

Given an input $\mathbf{F} \in \mathbb{R}^{C\times H\times W}$, the MCA module processes three parallel branches. The channel branch uses an identity mapping:

$$\mathbf{F}_C'' = \sigma(T_{\text{ex}}(T_{\text{sq}}(\mathbf{F}))) \otimes \mathbf{F}. \tag{3}$$

Spatial attention is captured by rotating features along height and width axes via $PM_W(\cdot)$ and $PM_H(\cdot)$:

$$\tilde{\mathbf{F}}_H = PM_W(\mathbf{F}), \quad \mathbf{F}_H'' = PM_W^{-1}(\sigma(T_{\text{ex}}(T_{\text{sq}}(\tilde{\mathbf{F}}_H))) \otimes \tilde{\mathbf{F}}_H). \tag{4}$$

$$\tilde{\mathbf{F}}_W = PM_H(\mathbf{F}), \quad \mathbf{F}_W'' = PM_H^{-1}(\sigma(T_{\text{ex}}(T_{\text{sq}}(\tilde{\mathbf{F}}_W))) \otimes \tilde{\mathbf{F}}_W). \tag{5}$$

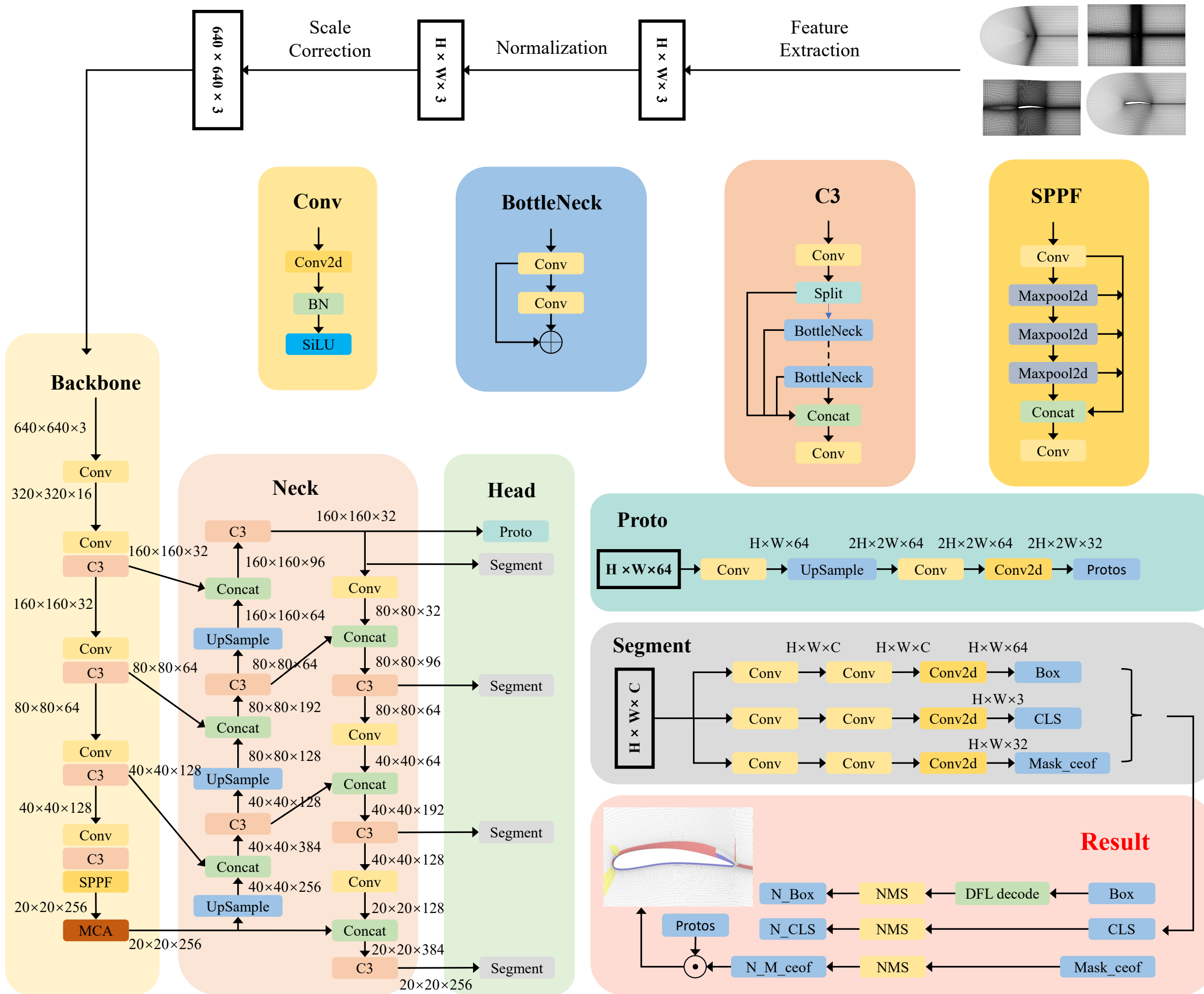

Fig. 5. Structural overview of the proposed FG-MeshNet algorithm.

The outputs are integrated via averaging:

$$\mathbf{F}'' = \frac{1}{3} \otimes \left(\mathbf{F}''_C \oplus \mathbf{F}''_H \oplus \mathbf{F}''_W\right). \tag{6}$$

The squeeze transformation T_{sq} adaptively fuses average and standard deviation pooling with trainable parameters α, β:

$$\hat{\mathbf{F}} = T_{\text{sq}}(\mathbf{F}) = \frac{1}{2} \otimes \left(\mathbf{F}^{\text{avg}} \oplus \mathbf{F}^{\text{std}}\right) \oplus \alpha \otimes \mathbf{F}^{\text{avg}} \oplus \beta \otimes \mathbf{F}^{\text{std}}, \tag{7}$$

where the excitation T_{ex} employs a 1D convolution with an adaptive kernel size K.

3) WIoU v3 loss function: To address annotation inconsistencies and varying sample quality in mesh evaluation, we adopt WIoU v3 as the regression loss. Its dynamic non-monotonic focusing mechanism distinguishes sample quality and mitigates detrimental gradient effects from poor annotations, enhancing robustness across diverse mesh morphologies. WIoU v3 employs an outlier assessment mechanism to perceive sample quality:

$$\beta = \frac{\mathcal{L}^*_{IoU}}{\overline{\mathcal{L}_{IoU}}}, \tag{8}$$

where $\overline{\mathcal{L}_{IoU}}$ is the exponential moving average of $\mathcal{L}_{IoU}$. The complete WIoU v3 loss is defined as:

$$\mathcal{L}_{WIoUv3} = r \cdot \mathcal{R}_{WIoU} \cdot \mathcal{L}_{IoU}, \tag{9}$$

where the distance attention weight $\mathcal{R}_{WIoU}$ and the gradient gain factor r are:

$$\mathcal{R}_{WIoU} = \exp\left(\frac{(x - x_{gt})^2 + (y - y_{gt})^2}{(W_g^2 + H_g^2)^*}\right), \tag{10}$$

$$r = \frac{\beta}{\delta \alpha^{\beta - \delta}}. \tag{11}$$

Here, α and δ are hyperparameters, and the superscript $(\cdot)^*$ indicates the variable is detached from the computation graph. This design suppresses the impact of annotation noise by reducing gradient gain for low-quality samples (large β), balances the learning focus across varying sample qualities, and enhances localization accuracy for poor-quality regions.

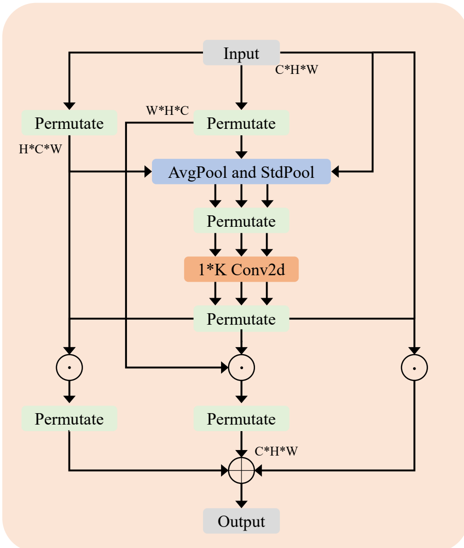

Fig. 6. Architecture of the MCA module.

IV. Experimental results

A. Training

All experiments were conducted on a Windows 11 workstation equipped with an NVIDIA GeForce RTX 4090 GPU, utilizing the PyTorch 2.7.0 framework and CUDA 12.8 toolkit. During preprocessing, the dataset was partitioned into training, validation, and test sets in a 8:1:1 ratio. The validation set was employed to monitor real-time performance and guide hyperparameter tuning to mitigate overfitting. To enhance the diversity of mesh representations, data augmentation techniques, including random rotation and mirroring, were applied during training. The input mesh resolution was standardized to 640×640, with a batch size of 64 and a total of 100 training epochs. We adopted a dynamic optimizer strategy: AdamW was utilized for the initial 10,000 iterations, automatically switching to SGD thereafter. The learning rate followed a cosine annealing schedule with warm-up, starting at an initial rate of 0.01.

B. Performance metrics

To evaluate the performance of FG-MeshNet, this paper adopts a fine-grained evaluation system focusing on three specific defect types: poor orthogonality, insufficient smoothness, and uneven density. These metrics measure the model's ability to accurately distinguish specific quality defects through macro-averaging, assessing its potential for detailed element-level evaluation. Precision and Recall are calculated for each defect type separately and then macro-averaged:

$$\text{Precision} = \frac{TP}{TP+FP}, \quad \text{Recall} = \frac{TP}{TP+FN}, \tag{12}$$

where True Positives (TP) are correctly identified defective cells, False Positives (FP) are qualified cells incorrectly identified as defective, and False Negatives (FN) are missed defective cells. The core metric, Mean Average Precision (mAP_{50}), is calculated at an IoU threshold of 0.5:

$$\text{mAP}_{50} = \frac{1}{C}\sum_{i=1}^{C} \text{AP}_{50,i}, \tag{13}$$

where $C = 3$ (representing the three defect categories) and $\text{AP}_{50,i}$ is the area under the precision-recall curve for each category.

C. Instance Segmentation Evaluation

Table II summarizes the quantitative performance on NACA-FineGrade, where FG-MeshNet achieves a mAP_{50} of 89.3%. The model demonstrates robust evaluation across specific categories: the MCA module enables high precision (96.2%) in smoothness defects by capturing subtle gradient variations, while orthogonality detection maintains exceptional precision (96.7%) and recall (97.0%). Although density recall (70.7%) is lower due to extreme aspect ratios in boundary layers, the high precision across critical categories ensures reliable guidance for element-level optimization.

Qualitative results in Fig. 7 further corroborate these findings, showing high mask consistency and a clear understanding of mesh semantic logic. Even in overlapping defect regions, the model accurately delineates boundaries, proving it transcends mere texture memorization. With only 2.637 million parameters, this lightweight architecture facilitates rapid inference and real-time integration into iterative optimization pipelines, effectively solving the "black box" bottleneck of existing intelligent evaluation methods.

D. Ablation Study on Core Modules

This section evaluates the core modules of FG-MeshNet through ablation studies. We analyze three critical design choices: the number of segmentation heads, the choice of attention mechanisms, and the regression loss functions. Due to the high computational cost of training on the full dataset, hyper-parameter optimization was conducted on a representative subset (1024 meshes of uniform size). Subsequent experiments on this subset quantify each component's contribution to the overall algorithm performance.

1) Effect of Segmentation Head Count: The number of segmentation heads is vital for balancing accuracy and efficiency across spatial scales. As shown in Table III, the 4-heads configuration yields superior performance (86.9% mAP_{50}) with the fewest parameters (2.637M). This paradox stems from a structural optimization: to incorporate the P2 scale for small defects, the model streamlines the backbone and neck by reducing block depth and channel width. This design prioritizes multi-scale spatial resolution over redundant channel density, providing a more comprehensive yet lightweight representation across varying defect scales.

2) Effect of Different Attention Modules: The MCA module is introduced for feature enhancement and compared against other attention mechanisms in Table IV. While SE [23] and ECA [24] improved mAP_{50} by 1.2% and 4.2% respectively

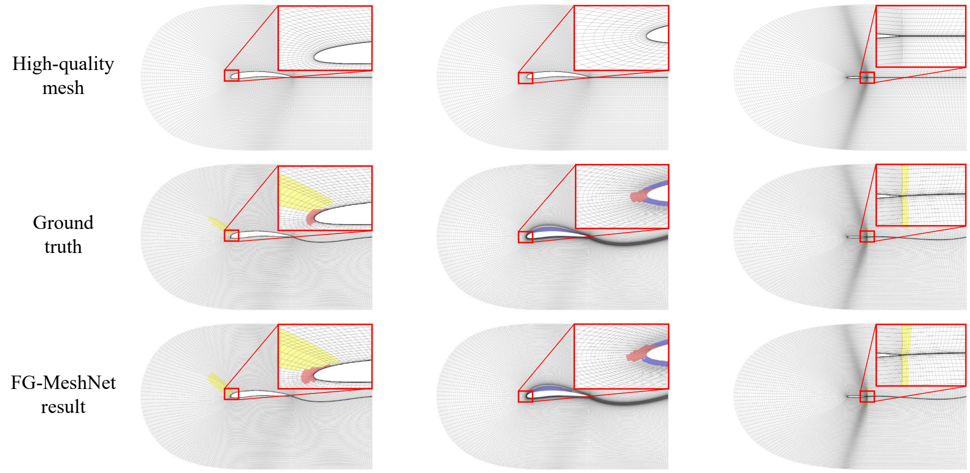

Fig. 7. Qualitative results of mesh quality evaluation by FG-MeshNet.

TABLE II
PERFORMANCE EVALUATION OF FG-MESHNET ON MESH INSTANCE SEGMENTATION.

Defect Type	Precision(%)	Recall(%)	mAP_{50}(%)	Average mAP_{50}(%)	Para(M)
Orthogonality	96.7	97.0	97.3	89.3	2.637
Smoothness	96.2	87.8	95.5		
Density	75.5	70.7	75.1		

TABLE III
TRADE-OFF BETWEEN ACCURACY AND PARAMETERS FOR DIFFERENT SEGMENTATION HEADS.

Numbers	mAP_{50}(%)	Para(M)
2 heads	72.9	2.886
3 heads	82.3	2.774
4 heads	**86.9**	**2.637**

TABLE V
INFLUENCE OF DIFFERENT LOSS FUNCTIONS ON MODEL PERFORMANCE.

Loss functions	Precision(%)	Recall(%)	mAP_{50}(%)
CIoU	91.3	82.5	87.2
EIoU	85.1	80.5	84.7
SIoU	90.5	**83.7**	86.0
WIoU v3	**92.1**	83.4	**87.9**

without sacrificing speed, the MCA module achieved the highest performance of 87.2%, representing a 5.9% improvement over the baseline and 0.5% over ECA. Consequently, the MCA module is selected to guide model training.

TABLE IV
COMPARATIVE STUDY OF VARIOUS ATTENTION MODULES.

Methods	mAP_{50}(%)
Baseline(YOLOv8)	82.3
+SE	83.3
+ECA	86.8
+MCA	**87.2**

3) Effect of Loss Function: Table V compares WIoU v3 with CIoU [25], EIoU [26], and SIoU [27] for defect segmentation. WIoU v3 achieved the best results—92.1% Precision and 87.9% mAP_{50}. Its dynamic non-monotonic focusing mechanism suppresses noisy annotations, ensuring precise localization of complex defect morphologies.

E. Performance Comparison of Different Models

To evaluate FG-MeshNet, comparative experiments were conducted against several models, including Mask R-CNN, YOLOv8, SOLO, SOLO v2, and YOLACT (Table VI). As shown in Fig. 8a, FG-MeshNet exhibits a robust convergence process, reaching a final loss of 0.0276. This efficient training translates to superior performance in Fig. 8b, where FG-MeshNet achieves a peak mAP of 87.9%, outperforming all baseline models. Among the competitors, Mask R-CNN remains competitive at 86.2%, followed by YOLOv8 (82.3%), SOLO (76.9%), and SOLO v2 (75.2%), while YOLACT reaches 65.9%. Notably, FG-MeshNet achieves these results with a significantly lower parameter count. These results highlight FG-MeshNet's effectiveness in element-level mesh evaluation.

TABLE VI
PERFORMANCE OF DIFFERENT MODELS.

Models	mAP_{50}(%)	Para(M)
Mask R-CNN	86.2	62.5
SOLO	76.9	36.124
SOLO v2	75.2	46.238
YOLACT	65.9	34.741
YOLOv8	82.3	2.774
FG-MeshNet	**87.9**	**2.637**

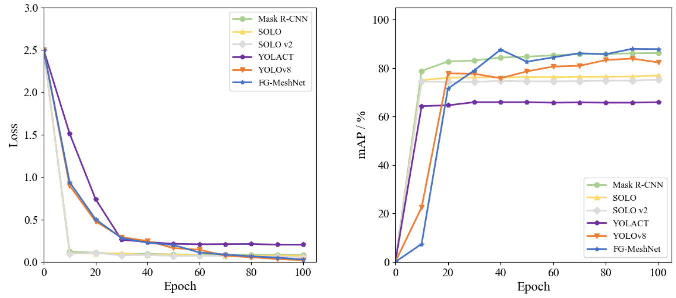

(a) Comparison of loss values.

(b) Comparison of mAP_{50}.

Fig. 8. Comparison of loss values and mAP_{50} across different models.

V. Conclusion

In this paper, we propose a fine-grained quality evaluation algorithm designed to identify specific mesh defects and provide actionable guidance for optimization. To support this, we establish the NACA-FineGrade dataset, the first publicly available, large-scale benchmark featuring comprehensive element-level quality annotations. This dataset fills a significant gap in the field, providing the essential foundation for intelligent evaluation models. Building on this foundation, we introduce FG-MeshNet, A fine-grained intelligent mesh quality evaluation algorithm.

The algorithm integrates a multi-scale feature fusion network, an MCA module for synergistic feature refinement, and the WIoU v3 loss function. Ablation studies confirmed the contribution of each component to the overall performance. FG-MeshNet achieved 89.3% mAP_{50} at the element-level, demonstrating its capability for precise defect localization.

Despite these advancements, the current application of our algorithm focuses on 2D airfoil meshes. Future work will expand the NACA-FineGrade dataset to include broader topologies and 3D geometries. We will also explore model compression and optimization techniques to further enhance the algorithm's efficiency, strengthening its role in advancing intelligent CFD pipelines.

References

[1] X. Chen, Z. Wang, L. Deng, J. Yan, C. Gong, B. Yang, Q. Wang, Q. Zhang, L. Yang, Y. Pang *et al.*, "Towards a new paradigm in intelligence-driven computational fluid dynamics simulations," *Engineering Applications of Computational Fluid Mechanics*, vol. 18, no. 1, p. 2407005, 2024.

[2] X. Gao, J. Huang, K. Xu, Z. Pan, Z. Deng, and G. Chen, "Evaluating hex-mesh quality metrics via correlation analysis," in *Computer graphics forum*, vol. 36, no. 5. Wiley Online Library, 2017, pp. 105–116.

[3] J. P. Slotnick, A. Khodadoust, J. Alonso, D. Darmofal, W. Gropp, E. Lurie, and D. J. Mavriplis, "Cfd vision 2030 study: a path to revolutionary computational aerosciences," Tech. Rep., 2014.

[4] X. Chen, J. Liu, Y. Pang, J. Chen, L. Chi, and C. Gong, "Developing a new mesh quality evaluation method based on convolutional neural network," *Engineering Applications of Computational Fluid Mechanics*, vol. 14, no. 1, pp. 391–400, 2020.

[5] X. Chen, C. Gong, J. Liu, Y. Pang, L. Deng, L. Chi, and K. Li, "A novel neural network approach for airfoil mesh quality evaluation," *Journal of Parallel and Distributed Computing*, vol. 164, pp. 123–132, 2022.

[6] Z. Wang, X. Chen, T. Li, C. Gong, Y. Pang, and J. Liu, "Evaluating mesh quality with graph neural networks," *Engineering with Computers*, vol. 38, no. 5, pp. 4663–4673, 2022.

[7] Z. Liu, H. Liu, Y. Chen, W. Zhang, W. Song, L. Zhou, Q. Wei, and J. Xu, "Evaluating airfoil mesh quality with transformer," *Aerospace*, vol. 10, no. 2, p. 110, 2023.

[8] H. Zhang, H. Li, X. Wu, and N. Li, "Mtgnet: multi-label mesh quality evaluation using topology-guided graph neural network," *Engineering with Computers*, vol. 41, no. 1, pp. 321–333, 2025.

[9] X. Chen, J. Liu, C. Gong, S. Li, Y. Pang, and B. Chen, "Mve-net: An automatic 3-d structured mesh validity evaluation framework using deep neural networks," *Computer-Aided Design*, vol. 141, p. 103104, 2021.

[10] X. Chen, Z. Wang, J. Liu, C. Gong, and Y. Pang, "A neural network-based mesh quality indicator for three-dimensional cylinder modelling," *Entropy*, vol. 24, no. 9, p. 1245, 2022.

[11] J. F. Thompson, B. K. Soni, and N. P. Weatherill, *Handbook of grid generation*. CRC press, 1998.

[12] M. Nguyen-Dinh, J. Peter, R. Sauvage, M. Meaux, and J.-A. Désidéri, "Mesh quality assessment based on aerodynamic functional output total derivatives," *European Journal of Mechanics-B/Fluids*, vol. 45, pp. 51–71, 2014.

[13] X. Chen, Z. Wang, Y. Liu, Y. Pang, B. Chen, J. Chen, C. Gong, and J. Liu, "A neural network approach for unstructured mesh quality evaluation," *Engineering Computations*, vol. 42, no. 6, pp. 2021–2035, 2025.

[14] K. He, G. Gkioxari, P. Dollár, and R. Girshick, "Mask r-cnn," in *Proceedings of the IEEE international conference on computer vision*, 2017, pp. 2961–2969.

[15] S. Liu, L. Qi, H. Qin, J. Shi, and J. Jia, "Path aggregation network for instance segmentation," in *Proceedings of the IEEE conference on computer vision and pattern recognition*, 2018, pp. 8759–8768.

[16] K. Chen, J. Pang, J. Wang, Y. Xiong, X. Li, S. Sun, W. Feng, Z. Liu, J. Shi, W. Ouyang *et al.*, "Hybrid task cascade for instance segmentation," in *Proceedings of the IEEE/CVF conference on computer vision and pattern recognition*, 2019, pp. 4974–4983.

[17] X. Wang, T. Kong, C. Shen, Y. Jiang, and L. Li, "Solo: Segmenting objects by locations," in *European conference on computer vision*. Springer, 2020, pp. 649–665.

[18] D. Bolya, C. Zhou, F. Xiao, and Y. J. Lee, "Yolact: Real-time instance segmentation," in *Proceedings of the IEEE/CVF international conference on computer vision*, 2019, pp. 9157–9166.

[19] H. Chen, K. Sun, Z. Tian, C. Shen, Y. Huang, and Y. Yan, "Blendmask: Top-down meets bottom-up for instance segmentation," in *Proceedings of the IEEE/CVF conference on computer vision and pattern recognition*, 2020, pp. 8573–8581.

[20] M. Sohan, T. Sai Ram, and C. V. Rami Reddy, "A review on yolov8 and its advancements," in *International Conference on Data Intelligence and Cognitive Informatics*. Springer, 2024, pp. 529–545.

[21] Y. Yu, Y. Zhang, Z. Cheng, Z. Song, and C. Tang, "Mca: Multidimensional collaborative attention in deep convolutional neural networks for image recognition," *Engineering Applications of Artificial Intelligence*, vol. 126, p. 107079, 2023.

[22] Z. Tong, Y. Chen, Z. Xu, and R. Yu, "Wise-iou: bounding box regression loss with dynamic focusing mechanism," *arXiv preprint arXiv:2301.10051*, 2023.

[23] J. Hu, L. Shen, and G. Sun, "Squeeze-and-excitation networks," in *Proceedings of the IEEE conference on computer vision and pattern recognition*, 2018, pp. 7132–7141.

[24] Q. Wang, B. Wu, P. Zhu, P. Li, W. Zuo, and Q. Hu, "Eca-net: Efficient channel attention for deep convolutional neural networks," in *Proceedings of the IEEE/CVF conference on computer vision and pattern recognition*, 2020, pp. 11 534–11 542.

[25] Z. Zheng, P. Wang, W. Liu, J. Li, R. Ye, and D. Ren, "Distance-iou loss: Faster and better learning for bounding box regression," in *Proceedings of the AAAI conference on artificial intelligence*, vol. 34, no. 07, 2020, pp. 12 993–13 000.

[26] Y.-F. Zhang, W. Ren, Z. Zhang, Z. Jia, L. Wang, and T. Tan, "Focal and efficient iou loss for accurate bounding box regression," *Neurocomputing*, vol. 506, pp. 146–157, 2022.

[27] Z. Gevorgyan, "Siou loss: More powerful learning for bounding box regression," *arXiv preprint arXiv:2205.12740*, 2022.